nature nanotechnology

SUPPLEMENTARY INFORMATION

https://doi.org/10.1038/s41565-020-0712-7

In the format provided by the authors and unedited.

A Josephson phase battery

Elia Strambini[1]✉, Andrea Iorio[1]✉, Ofelia Durante[2], Roberta Citro[2], Cristina Sanz-Fernández[3], Claudio Guarcello[2,3], Ilya V. Tokatly[4,5], Alessandro Braggio[1], Mirko Rocci[1,7], Nadia Ligato[1], Valentina Zannier[1], Lucia Sorba[1], F. Sebastián Bergeret[3,6]✉ and Francesco Giazotto[1]✉

[1]NEST, Istituto Nanoscienze-CNR and Scuola Normale Superiore, Pisa, Italy. [2]Dipartimento di Fisica 'E. R. Caianiello', Università di Salerno, Fisciano, Italy. [3]Centro de Física de Materiales (CFM-MPC), Centro Mixto CSIC-UPV/EHU, San Sebastián, Spain. [4]Nano-Bio Spectroscopy Group, Departamento de Física de Materiales, Universidad del País Vasco (UPV/EHU), Donostia-San Sebastián, Spain. [5]Ikerbasque, Basque Foundation for Science, Bilbao, Spain. [6]Donostia International Physics Center (DIPC), San Sebastián, Spain. [7]Present address: Francis Bitter Magnet Laboratory and Plasma Science and Fusion Center, Massachusetts Institute of Technology, Cambridge, MA, USA. ✉e-mail: elia.strambini@sns.it; andrea.iorio@sns.it; fs.bergeret@csic.es; francesco.giazotto@sns.it

Supplementary Information for "A Josephson phase battery"

E. Strambini, A. Iorio, O. Durante, R. Citro, C. Sanz-Fernández, C. Guarcello, I. V. Tokatly, A. Braggio, M. Rocci, N. Ligato, V. Zannier, L. Sorba, F.S. Bergeret, and F. Giazotto

DEVICE FABRICATION

Hybrid proximity DC SQUIDs devices were fabricated starting from gold catalyzed n-doped InAs nanowires with typical length of 1.5 µm and a diameter of $\sim$ 85 nm grown by chemical beam epitaxy [1]. The n-doping was obtained with Se [2] and the metalorganic precursors for the nanowire growth was trimethylindium (TMIn), tertiarybutylarsine (TBAs) and ditertiarybutylselenide (DTSe), with line pressures of 0.6, 1.5 and 0.3 Torr respectively. Nanowires were drop-casted onto a substrate consisting of 300 nm thick SiO_2 on p-doped Si. Afterwards, a 280 nm-thick layer of positive-tone Poly(methyl methacrylate) (PMMA) electron beam resist was spun onto the substrate. The devices were then manually aligned to the randomly distributed InAs nanowires and patterned by means of standard electron beam lithography (EBL) followed by electron beam evaporation (EBE) of superconducting Ti/Al (5/100 nm) electrodes. Low-resistance ohmic contacts between the superconducting leads and the InAs nanowires were promoted by exposing the InAs nanowire contact areas to a highly diluted ammonium polysolfide $(NH_4)S_x$ solution, which selectively removes the InAs native oxide and passivates the surface, prior to EBE. The fabrication process was finalized by dissolving the PMMA layer in acetone.

From transport characterization on similar wires and normal metal electrodes [3], we estimate a typical electron concentration $n \simeq 2 \times 10^{18}\,\mathrm{cm}^{-3}$ and mobility $\mu \simeq 1200\,\mathrm{cm}^2/\mathrm{Vs}$. The corresponding Fermi velocity v_F, mean free path l_e and diffusion coefficient $D = v_F l_e/3$, are evaluated to be $v_F \simeq 2 \times 10^6\,\mathrm{m/s}$, $l_e \simeq 30\,\mathrm{nm}$ and $D \simeq 200\,\mathrm{cm}^2/\mathrm{s}$.

I. KONDO RESISTANCE $R(T)$

To quantify the amount of unpaired spins in our system the temperature dependence of the normal-state resistance $R(T)$ has been studied in the range 10 K to 300 K. The data exhibits an upturn at $T \sim 80\,\mathrm{K}$ (see Fig. S1) suggesting a Kondo scattering mechanisms between the free electrons and the unpaired spins in the weak-links. Since the InAs nanowires were synthesized without incorporating any magnetic impurity (to the best of our knowledge, Se doping cannot

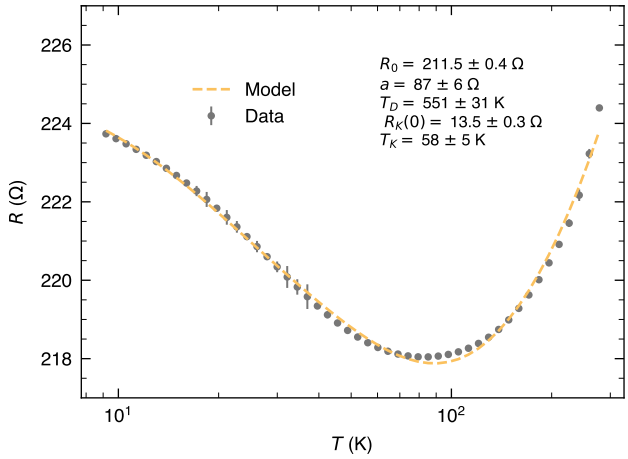

FIG. S1. **Kondo upturn of the InAs nanowire**. Resistance vs temperature $R(T)$ of one of the devices measured during the cooldown of the refrigerator showing a clear increase of resistance for temperature below 80 K. This behaviour is consistent with the Kondo scattering model as demonstrated by the good fit of the $R-T$ data with the model in Eq. S3.

provide by itself any magnetism), we conjecture that unpaired spins are originated from oxides states at the nanowire surface, in analogy with what is observed in metallic nanowires [4, 5]. Indeed, the $R(T)$ of a diluted magnetic alloy follows the universal non-monotonic relation [6]

$$R(T) = R_0 + R_{el-ph}(T) + R_K(T), \tag{S1}$$

where R_0 is the residual resistance while $R_{el-ph}(T)$ and $R_K(T)$ are the contribution given respectively by the electron-phonon and the Kondo scattering. The temperature dependence of the former can be expressed according to the Bloch-Gruneisen model as [7]

$$R_{el-ph}(T) = a\left(\frac{T}{\theta_D}\right)^5 \int_0^{\theta_D/T} \frac{x^5}{(e^x-1)(1-e^{-x})}\mathrm{d}x. \tag{S2}$$

For the Kondo contribution many analytical approximations are available according to the range of temperature investigated. In the full range of temperature the exact solution exist from the numerical renormalization group theory (NRG). In the following we use an empirical fitting function derived as an analytical approximation of the NRG given by [8–11]

$$R_K^{NRG} = R_K(0)\left(\frac{T_K'^2}{T^2+T_K'^2}\right)^s, \tag{S3}$$

with T_K' related to the actual Kondo temperature T_K by $T_K' = T_K/(2^{1/s}-1)^{1/2}$. Note that Eq. S3 is defined such that $R_K(T_K) = R_K(0)/2$ and the parameter s is fixed to $s = 0.22$ as expected

for a spin 1/2 impurity. In Fig. S1 we show the fit of the experimental data with Eq. S3, from which we extract a Kondo temperature $T_K = 58 \pm 5$ K, a residual magnetic impurity resistance $R_K(0) = 13.5 \pm 0.3\ \Omega$, a coefficient $a = 87 \pm 6\ \Omega$ and a Debye temperature $\theta_D = 551 \pm 31$ K. From $R_K(0)$ is possible to estimate the density of unpaired spin, that form the Hamann expression of the residual Kondo resistance in the unitary limit is given by [12]

$$R_K(0) = \frac{L}{A}\frac{4\pi c\hbar}{nk_F e^2}, \tag{S4}$$

with $L \sim 80\,\text{nm}$ junction lenghts, $A \sim \pi r^2$ with $r \sim 45\,\text{nm}$ nanowire cross-sectional area, k_F Fermi wavevector and n electron carrier density, from which we estimate the density of magnetic impurities $c \simeq 1.36 \times 10^{17}\,\text{cm}^{-3}$. This corresponds to a concentration of ~ 4 ppm ($= c/n_{InAs}$, with the InAs atomic density $n_{InAs} = 3.59 \times 10^{22}\,\text{cm}^{-3}$) of unpaired spins in the InAs nanowire .

II. FIRST "MAGNETIZATION" CURVE

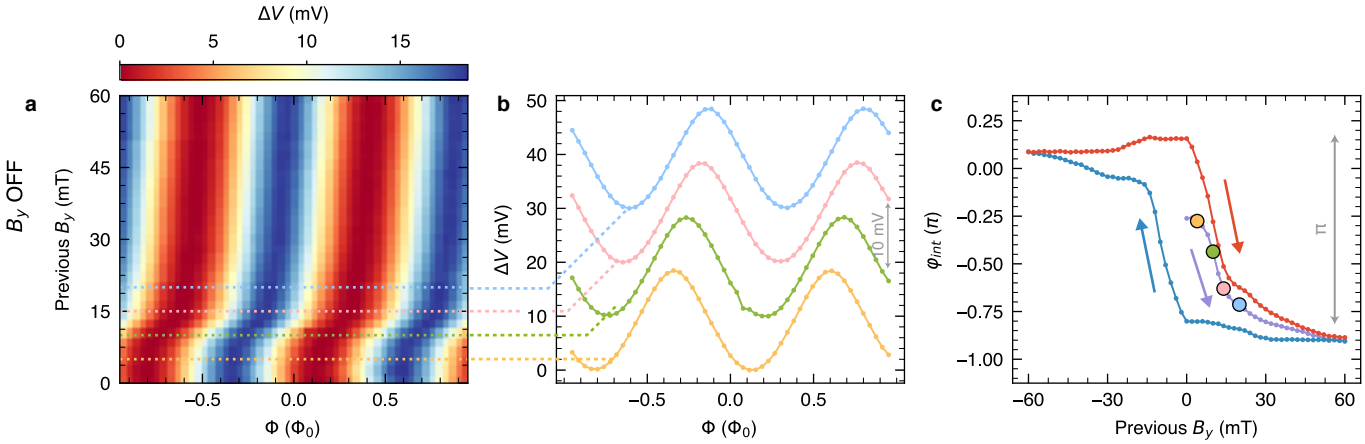

FIG. S2. **First magnetization curve of φ_{int}.** **a**, Color plot of the voltage drop $\Delta V(\Phi)$ measured at $B_y = 0$ after the magnetic field was swept to the values shown on the y-axis straight after the thermal cycle. **b**, Selected traces $\Delta V(\Phi)$ corresponding to the cuts in **a**. **c**, Intrinsic phase shift φ_{int} extracted from **b**, showing the first polarization of the unpaired spins (violet curve) and the hysteresis loop followed in the subsequent back and forth sweeps of B_y, blue and red curves, respectively.

The persistent hysteretic loops of the φ_0-shift, shown in Fig. 1d-f of the main text, are consistent with the presence of a ferromagnetic background of unpaired spin. To support this hypothesis, we show in Fig. S2a and b the first magnetization curve of this spin ensemble measured in the same device. Initially, the magnetization of the sample is lifted by warming the system above 3 K. Then,

the SQUID voltage drop $\Delta V(\Phi)$ is measured in the absence of the in-plane magnetic field B_y which is gradually turned on thus polarizing the unpaired spins. The resulting $\Delta V(\Phi)$ shows no shifts at low B_y while, only above 5 mT a clear shift is generated. The resulting φ_{int} extracted by fitting $\Delta V(\Phi)$ is shown in the violet curve of Fig. S2c. By reversing B_y the φ_{int} then evolves with the typical hysteretic curve of a ferromagnetic system (blue and red curves in Fig. S2c).

III. SQUID WITH ANOMALOUS JOSEPHSON JUNCTIONS

The critical current of a SQUID interferometer can be evaluated from the CPR of the two JJs forming the interferometer. Using a sinusoidal CPR, the currents through the two junctions can be written as

$$i_1 = I_c \sin\left[(\varphi_C - \varphi_L) + \varphi_0^{(1)}\right] \qquad i_2 = I_c \sin\left[(\varphi_C - \varphi_R) + \varphi_0^{(2)}\right], \tag{S5}$$

where $\varphi_L, \varphi_C, \varphi_R$ are the left,central and right superconducting phases and I_c is the critical current of each JJ.

The supercurrent of the SQUID is the sum of the two contributions ($I_s = i_1 + i_2$,) and, with the constraint on the superconducting phases of the flux quantization

$$(\varphi_L - \varphi_C) + (\varphi_C - \varphi_R) + 2\pi\frac{\Phi}{\Phi_0} = 2\pi \text{ (mod n)}, \tag{S6}$$

it has the form

$$I_s = 2I_C \sin(\delta_0) \cos\left[\frac{1}{2}\left(2\pi\frac{\Phi}{\Phi_0} + \varphi_{tot}\right)\right], \tag{S7}$$

where $\delta_0 = \varphi_C - \frac{\varphi_L+\varphi_R}{2} + \frac{(\varphi_0^{(2)}+\varphi_0^{(1)})}{2}$ and $\varphi_{tot} = \varphi_0^{(2)} - \varphi_0^{(1)}$ is the total anomalous phase built in the interferometer. With the geometry depicted in Fig. S3a, the two junctions experience the same in-plane magnetic field orientation but the supercurrents flow in opposite directions resulting in $\varphi_0^{(1)} = -\varphi_0^{(2)} = \varphi_0$ and $\varphi_{tot} = 2\varphi_0$. The stable state configuration of the SQUID is achieved by minimizing the total Josephson free energy obtained at $\delta_0 = \pi/2$, and then the maximum sustainable supercurrent results to be

$$I_S(\Phi) = 2I_C \left|\cos\left(\pi\frac{\Phi}{\Phi_0} + \frac{\varphi_{tot}}{2}\right)\right|. \tag{S8}$$

It follows that in absence of magnetic flux, the maximum supercurrent is reduced by a factor $\sim |\cos(\varphi_{tot}/2)|$ compared to the non-anomalous case as a consequence of the anomalous supercurrent already present in the interferometer. In a more conventional geometry as the one showed in Fig. S3b, the anomalous phases acquired by the two junctions would be the same $\varphi_0^{(1)} = \varphi_0^{(2)} = \varphi_0$, making impossible its detection in the phase-to-current readout employed in the present work.

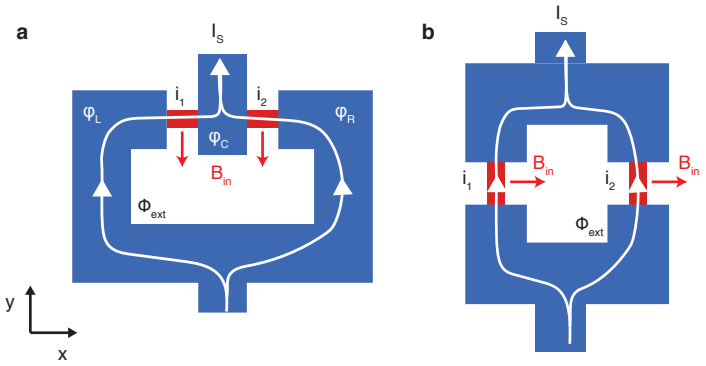

FIG. S3. **Comparison between SQUID geometries.** The SQUID geometry employed in this work **a** allows a simple readout of the anomalous phase φ_{tot} generated by a uniform magnetic field B_{in} since the opposite direction of the supercurrents in the two JJs. This would not be possible in a conventional geometry as the one shown in **b**.

IV. LATERAL φ_0-JUNCTION

The origin of the anomalous phase φ_0 is the singlet-triplet conversion mediated by the spin-orbit coupling (SOC), which in the normal state corresponds to the charge-spin conversion [13]. The calculations of the anomalous Josephson current in φ_0-junctions have been done for ideal planar S-N-S junctions, in which the superconducting electrodes and the normal region with SOC are separated by sharp boundaries [13–15], where the singlet-triplet coupling takes place only at N region. As shown in Ref. [13], this assumption leads to a monotonically increase of the anomalous phase φ_0 as a function of the applied magnetic field, which contrasts with curves extracted from our experiment (see Fig. 3a in the main text). It is however clear that our experimental setup (Fig. 1 in the main text) differs from an ideal S-N-S junction. Indeed, in each junction, the superconducting leads are covering part of the wires over distances larger than the coherence length. This means that the SOC, and hence the spin-charge conversion, is also finite in the portion of the wire covered by the superconductor. As we show in this section, this feature is essential to understand the experimental findings; in particular, the dependence to φ_0 from the external magnetic field. In this calculation, we focus on the dependence of φ_0 on the y direction of the field, i.e., B_{in} at $\theta = \pi/2$ (see Figs. 3a and b in the main text).

To be specific, we consider the junction sketched in Fig. S4. We assume an infinite diffusive quasi-one dimensional nanowire along the x-axis, which is partially covered by two semi-infinite Al superconducting leads at $x < L/2$ and $x > L/2$. We assume, for simplicity, that the proximity effect is weak and that the wire is diffusive. In such a case, the condensate function, which determines the

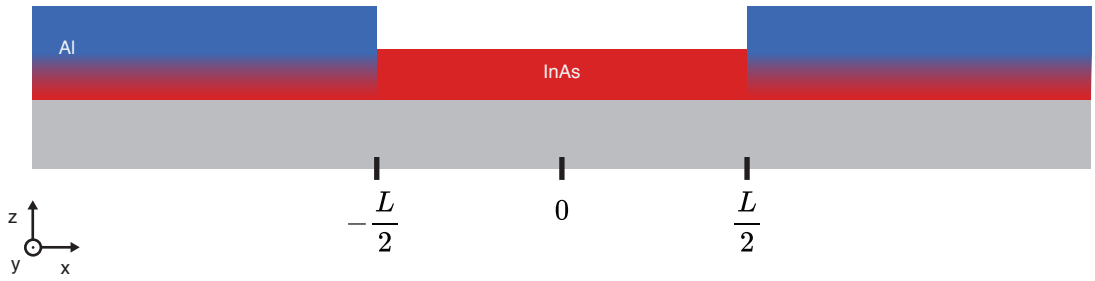

FIG. S4. **Schematic view of the S-N-S junctions.** At $|x| > L/2$, the InAs nanowire (red region) is partially covered by the Al superconducting leads (dark blue regions). The gray region corresponds to the substrate. This schematic view corresponds to the z-x plane of Fig. 3b (top panel) in the main text.

Josephson current, obeys the linearized Usadel equation, which results in two coupled differential equations for the singlet and triplet components as shown in Ref. [13]. Because the wire lies on a substrate plane, the system has an uniaxial asymmetry in the z direction perpendicular to the substrate (see Fig. S4). In the presence of SOC, this allows for a gradient singlet-triplet coupling generated by a differential operator of the form $C_k^a \partial_k \sim (\hat{z} \times \nabla)^a$, which converts a scalar (the singlet) into a pseudovector (the triplet) and vice-versa [13, 14]. We consider the case when the external field is applied in the y direction, and hence, the superconducting condensate function has the form $f = f_s + i f_t \mathrm{sgn}\omega \sigma^y$, where $f_{s,t}$ are the singlet and triplet components and ω the Matsubara frequency. The linearized Usadel equation reads:

$$\begin{aligned} \frac{D}{2}\nabla^2 f_s - |\omega| f_s + (h - iD\kappa_{\mathrm{sc}}\partial_x)\, f_t = 0\,, \\ \frac{D}{2}\nabla^2 f_t - |\omega| f_t - (h - 2iD\kappa_{\mathrm{sc}}\partial_x)\, f_s = 0\,. \end{aligned} \tag{S9}$$

Here D is the diffusion coefficient and $h = \mu_{\mathrm{B}} g_{\mathrm{s}} B_{\mathrm{in}}/2$ is the Zeeman field. The last term in both equations describes the spin-charge conversion due to the SOC. It is proportional to the effective inverse length κ_{sc} and the spatial variation of the condensate in the direction of the wire axis. The form of this term is determined by the uniaxial anisotropy of the setup in combination with the fact that we assume that the field is applied only in y direction.

Equation (S9) is written for the full 3D geometry. To obtain an effective 1D Usadel equation, we integrate Eq. (S9) over the wire cross-section and use boundary conditions imposed on the condensate function at the surface of the wire. In the part of the wire which is covered by the superconductor, the interface between the wire and the superconductor is described by the linearized Kupryianov-Lukichev boundary condition:

$$\partial_x f_s|_{\mathrm{InAs/Al}} = \gamma f_{\mathrm{BCS}} e^{i\phi}, \tag{S10}$$

where γ is a parameter describing the InAs/Al interface, $f_{\rm BCS} = \Delta/\sqrt{\omega^2+\Delta^2}$ is the BCS bulk anomalous Green's function in the superconducting leads, and ϕ is the phase of the corresponding lead. In the uncovered parts of the wire, we impose a zero current flow which corresponds to $\partial_x f_{s/t}\big|_{\rm InAs/vac.} = 0$. The integration of Eq. (S9) over the cross-section of the wire results in two coupled equations for the singlet and triplet components:

$$\begin{aligned} &\partial_x^2 f_s - \kappa_\omega^2 f_s + \left(\kappa_h^2 - 2i\kappa_{\rm sc}\partial_x\right) f_t = S(x) \ , \\ &\partial_x^2 f_t - \kappa_\omega^2 f_t - \left(\kappa_h^2 - 2i\kappa_{\rm sc}\partial_x\right) f_s = 0 \ , \end{aligned} \tag{S11}$$

with

$$S(x) = \gamma f_{\rm BCS}\left[\Theta\left(x-\frac{L}{2}\right)e^{i\frac{\varphi}{2}} + \Theta\left(-x-\frac{L}{2}\right)e^{-i\frac{\varphi}{2}}\right] \ , \tag{S12}$$

$\kappa_\omega^2 = \frac{2|\omega|}{D}$, $\kappa_h^2 = \frac{2h}{\hbar D}$, and φ is the phase difference between these two Al leads. After a cumbersome but straightforward procedure, we solve Eq. (S11) for continue and finite $f_{s,t}$. From the knowledge of the singlet and triplet components one determines the Josephson current as follows [13]:

$$j(x) = \frac{\pi\sigma_{\rm D}T}{e}\sum_\omega \mathbb{I}{\rm m}\{f_s^*\partial_x f_s - f_t^*\partial_x f_t - i\kappa_{\rm sc}\left(f_s^* f_t + f_s f_t^*\right)\} \ . \tag{S13}$$

The resulting current can be written as $j = I_c\sin(\varphi+\varphi_0)$, with the anomalous-phase given by:

$$\varphi_0 = \arctan\left\{\frac{\sum_\omega \mathbb{I}{\rm m}\left\{f_{\rm BCS}^2 e^{-qL}\frac{\sinh(\kappa_{\rm sc}L)(q^2+\kappa_{\rm sc}^2)+2q\kappa_{\rm sc}\cosh(\kappa_{\rm sc}L)}{q(q^2-\kappa_{\rm sc}^2)^2}\right\}}{\sum_\omega \mathbb{R}{\rm e}\left\{f_{\rm BCS}^2 e^{-q^*L}\frac{\cosh(\kappa_{\rm sc}L)(q^{*2}+\kappa_{\rm sc}^2)+2q^*\kappa_{\rm sc}\sinh(\kappa_{\rm sc}L)}{q^*(q^{*2}-\kappa_{\rm sc}^2)^2}\right\}}\right\} \ , \tag{S14}$$

where $q^2 = \kappa_\omega^2+\kappa_{\rm sc}^2-i\kappa_h^2$. In order to compare with the experimental data, we assume a Rashba-like SOC and use the expression derived in Ref. [13] for the spin-charge coupling parameter, namely $\kappa_{\rm sc} = 2\tau\alpha^3 m^{*2}/\hbar^5$. By using typical values for the parameters of a InAs/Al system: $\xi_0 \simeq 100\,$nm, $\Delta \simeq 150\,\mu$eV, $m^* = 0.023\ m_e$, $T \simeq 25\,$mK, $g_s \simeq 12$, and $\alpha \simeq 0.24\,$eV Å, we find the $\varphi_0(B_{in})$ dependence corresponding to the one shown in Fig. 3a of the main text. We see that our model provides a good qualitative explanation of the two main observed features. Namely, the linear increase of φ_0 for small fields and a kind of saturation at $\varphi_0 \approx \pm 0.5\pi$.

In Fig. S5, we show different $\varphi_0(B_{in})$ curves obtained from our general expression (S14). Whereas for small fields the experimental slope (dashed grey line) can be obtained from different values of the parameters, the behaviour of φ_0 at larger fields depends strongly on these parameters.

Indeed, it is important to emphasize that the saturation value at $\varphi_0 \approx \pm 0.5\pi$ is not an universal property of the phase-battery. This value depends on the intrinsic properties of the system. In particular, larger values of the SOI α leads to larger values of $\varphi_{\rm ex}$ at values of the field larger

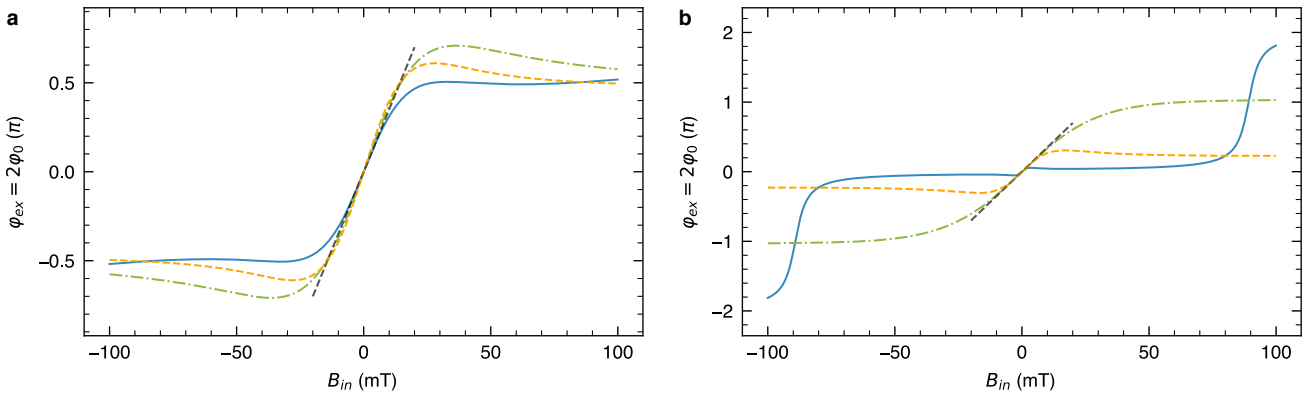

FIG. S5. **Theoretical model of the extrinsic anomalous phase.** The dependence of the extrinsic anomalous-phase on the magnetic field applied in y direction (B_{in} at $\theta = \pi/2$) for a) different temperatures, with $\alpha \simeq 0.24\,\text{eV Å}$ and for b) different values of α, with $T \simeq 10\,\text{mK}$. In a), the solid blue line coincides with the one shown in Fig. 3a of the main text, with $T \simeq 25\,\text{mK}$ and $g_s \simeq 12$. For the dashed orange line, we choose $T \simeq 10\,\text{mK}$ and $g_s \simeq 5$, and for the dashed-dotted line, $T \simeq 5\,\text{mK}$ and $g_s \simeq 2$. In b), the solid blue line corresponds to $\alpha \simeq 0.1\,\text{eV Å}$ and $g_s \simeq 37$, the dashed orange line to $\alpha \simeq 0.18\,\text{eV Å}$ and $g_s \simeq 7$, and the dashed-dotted green line to $\alpha \simeq 0.4\,\text{eV Å}$ and $g_s \simeq 3$. In both a) and b), the dashed grey line corresponds to the measured slope at low fields.

than those accessed in the experiment. This is shown in Fig. (S5)b, where we plot the $\varphi_0(B_{in})$ dependence for different values of α, with $T \simeq 10\,\text{mK}$. As in Fig. (S5)a, we change the g_s value to maintain the experimental slope in the low-field region. The linear behavior for the low-field region is shared by all the $\varphi_0(B_{in})$ curves, as shown in Fig. (S5). In this regime, we can thus find the slope value by linearizing Eq. (S14):

$$\varphi_0 \simeq C_1 B_{in} + O(B_{in}^3), \tag{S15}$$

with $C_1 \simeq 0.035\,\pi/\text{mT}$, which is in agreement with the value extracted from the experiment.

V. TRIVIAL MECHANISMS TO INDUCE PHASE SHIFTS

Trivial hypotheses, alternative to the anomalous φ_0 effect, have been also considered for the for the generation of a hysteretic phase shift: trapped magnetic fluxes and Abrikosov vortices.

- Trapped magnetic fluxes can be observed in superconducting loops with a non negligible ring inductance L and, more precisely, for a screening parameter $\beta_L = \frac{2\pi L I_c}{\Phi_0} \gtrsim 1$, with I_C being the critical current of a single junction [16]. This indeed can lead to a hysteretic behavior

due to the presence of a circulating current in the ring. For our interferometer we estimated $\beta_L \lesssim 10^{-2}$ ($I_C \sim 300\,\mathrm{nA}$ and $L \sim 10\,\mathrm{pH}$ [17]) that is very unlikely to induce any magnetic hysteresis. Still, if circulating currents are present, hysteretic jumps should be sharp, periodic and visible even at low B_z. The absence of any hysteretic behavior at low magnetic field is further confirmed by the continuous interference patterns shown in Figs. 1e and 1f.

- Abrikosov vortices, also known as fluxons, can be often induced in type-II superconductors – like the thin Al film used in our SQUID devices – when an out-of-plane magnetic field is applied. To avoid vortex intrusion into the ring surface, which might induce a parasitic phase shift, we limit our out-of-plane component to $|B_z| < 0.8\,\mathrm{mT}$, which guarantees the absence of any fluxon. Indeed, upon the application of a larger field $B_z \gtrsim (3-4)$ mT, also in our case abrupt phase shifts appear with a density that increases by increasing B_z, as shown in Fig. S6. This is what is expected for fluxons pinning in the Al, i.e., stochastic and

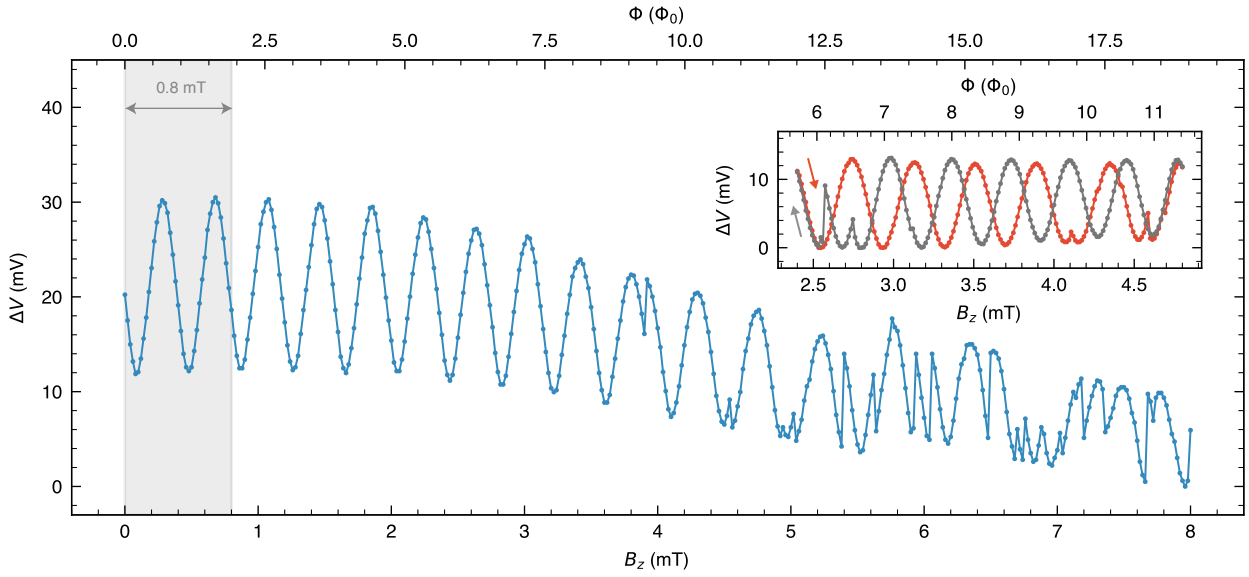

FIG. S6. **Fluxons induced phase shifts at high B_z.** Voltage drop $\Delta V(B_z)$ across the SQUID for $I_{sd} = 1\,\mu\mathrm{A}$ vs applied magnetic field B_z up to 8 mT recorded at $T = 100\,\mathrm{mK}$. The grey area indicated in the plot (corresponding to $0 \leq B_z \leq 0.8\,\mathrm{mT}$) is the one used to track and evaluate the induced phase shift in our interferometer. For $B_z \gtrsim 3\,\mathrm{mT}$ abrupt jumps in the phase start to appear due to trapped fluxons piercing the SQUID area. Inset: back (gray) and forth (red) traces at high B_z in the same conditions as before show an hysteretic behavior which is expected for fluxons pick-up.

abrupt events providing a discrete jump of the phase [18]. Notice also the hysteretic behavior expected for fluxon inclusion, which is underlined in the inset of the figure showing a local

back and forth measurement.

With respect to the in-plane magnetic fields, the thickness of the Al film (thinner than the superconducting coherence length) ensures the complete penetration of the magnetic field, and thereby the absence of generated fluxons. This is consistent with the lack of any stochastic shift upon the application of B_{in}.

VI. SUPPLEMENTARY DEVICE MEASURED

In this section we repeated the same magnetic characterization of the Josephson phase battery shown in Fig. 2 and 3 of the main text, performed on a different device to demonstrate the high reproducibility of the effect, apart sample-specific details. Notice that the behaviour of φ_{tot} and φ_{int} (Fig. S7) is qualitatively similar, but with a smaller total phase shift of $\sim 0.4\pi$ stemming for a weaker exchange interaction induced by the unpaired-spin. Moreover the angle dependence of $\varphi_{ex}(\theta)$ shown in Fig. S8 is in very good agreement with the evolution observed in Fig. 2 and expected from the model presented in Section IV.

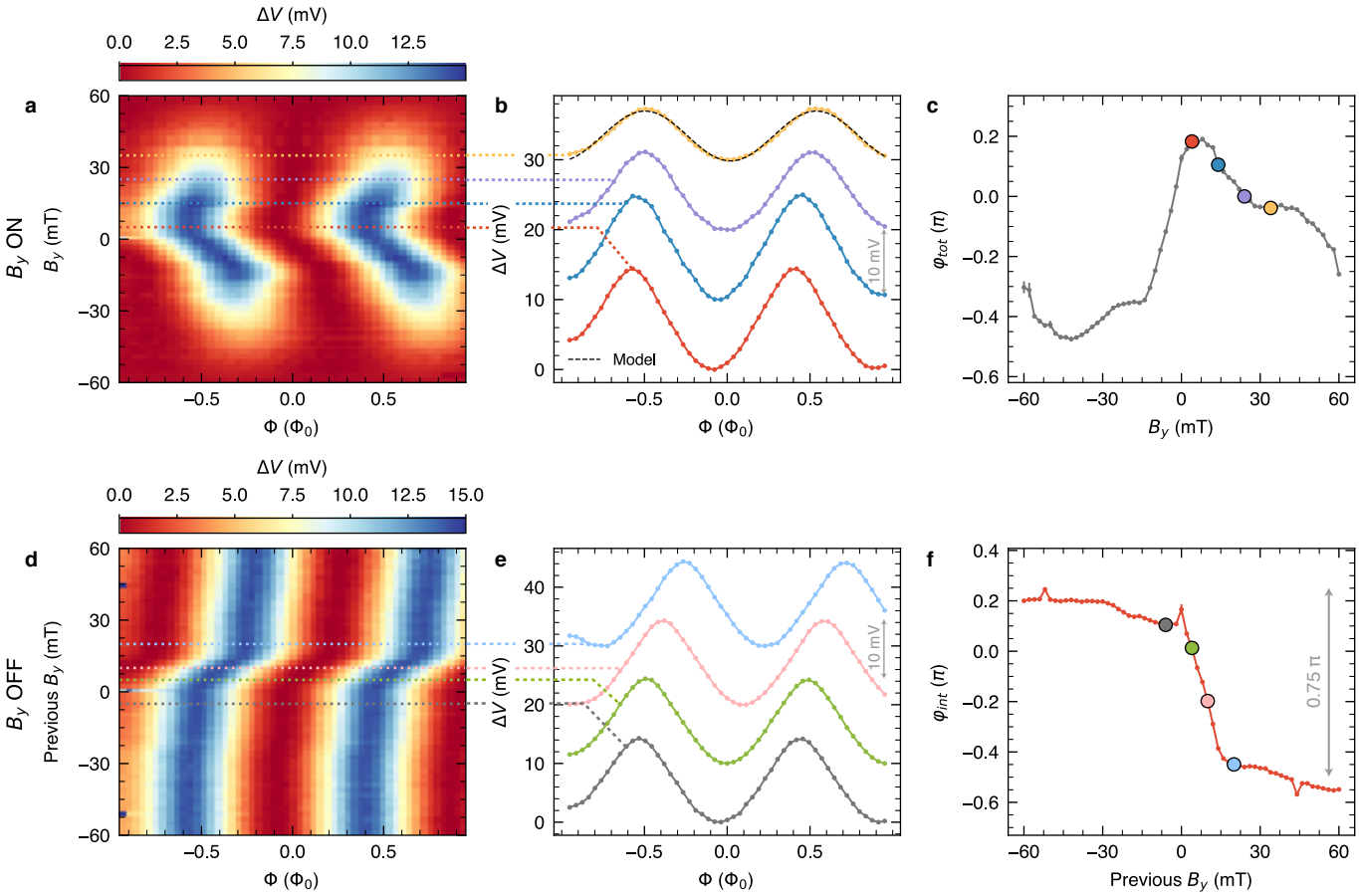

FIG. S7. **Charging loops of the Josephson phase battery (second device). a,** Voltage drop $\Delta V(\Phi)$ at constant current bias $I = 1\,\mu A$ vs in-plane magnetic field B_y applied orthogonal to the nanowire axis . At large $|B_y|$, the amplitude of $\Delta V(\Phi)$ is lowered due to the suppression of superconductivity inside the wire. Each trace is vertically offset for clarity. **b,** Selected traces $\Delta V(\Phi)$ extracted from **a** for different B_y. Data are vertically offset for clarity. **c,** Extracted phase shift φ_{tot} from the curves in **a**. **d,** Color plot of the persistent voltage drop $\Delta V(\Phi)$ measured at $B_y = 0$ after the magnetic field was swept to the values shown on the y-axis. **e,** Selected traces $\Delta V(\Phi)$ corresponding to the cuts in **d**. **f,** Intrinsic phase shift φ_{int} extracted from **d**. φ_{int} stems from the ferromagnetic polarization magnetic impurities. All data were recorded at 30 mK of bath temperature.

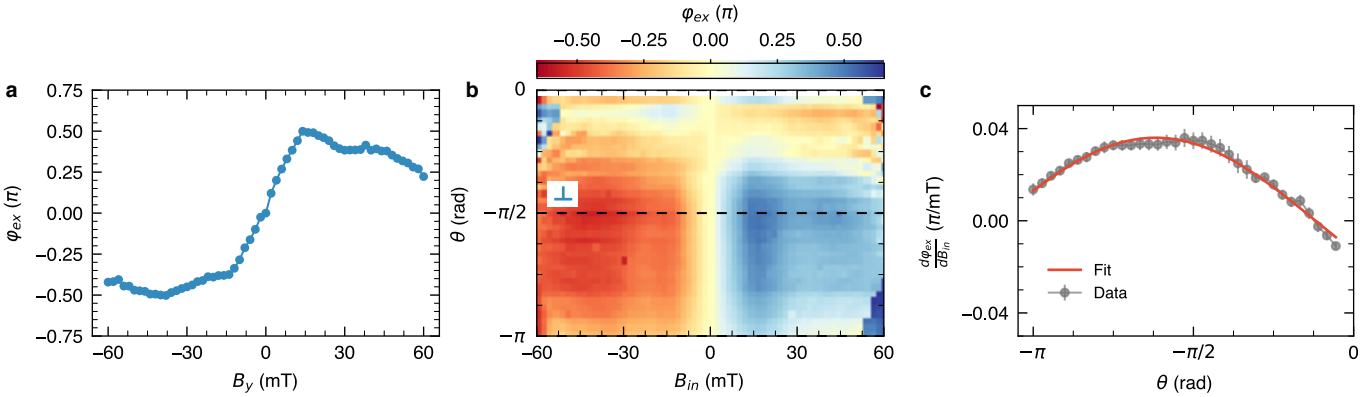

FIG. S8. **Vectorial symmetry of the anomalous phase φ_0 (second device). a,** Dependence of the extrinsic anomalous phase φ_{ex} on B_y. **b,** Evolution of the anomalous phase φ_{ex} on θ and B_{in}. **c,** $d\varphi_{ex}/dB_{in}$ vs θ together with a sinusoidal fit (red curve) from Eq. (S15). The slope has been evaluated by a linear fit of the data in **b** for $|B_{in}| < 10\,\mathrm{mT}$. The error bar is the RMS of the fit. All the data were recorded at 30 mK of bath temperature.

VII. LOW MAGNIFICATION SEM IMAGE OF THE DEVICE

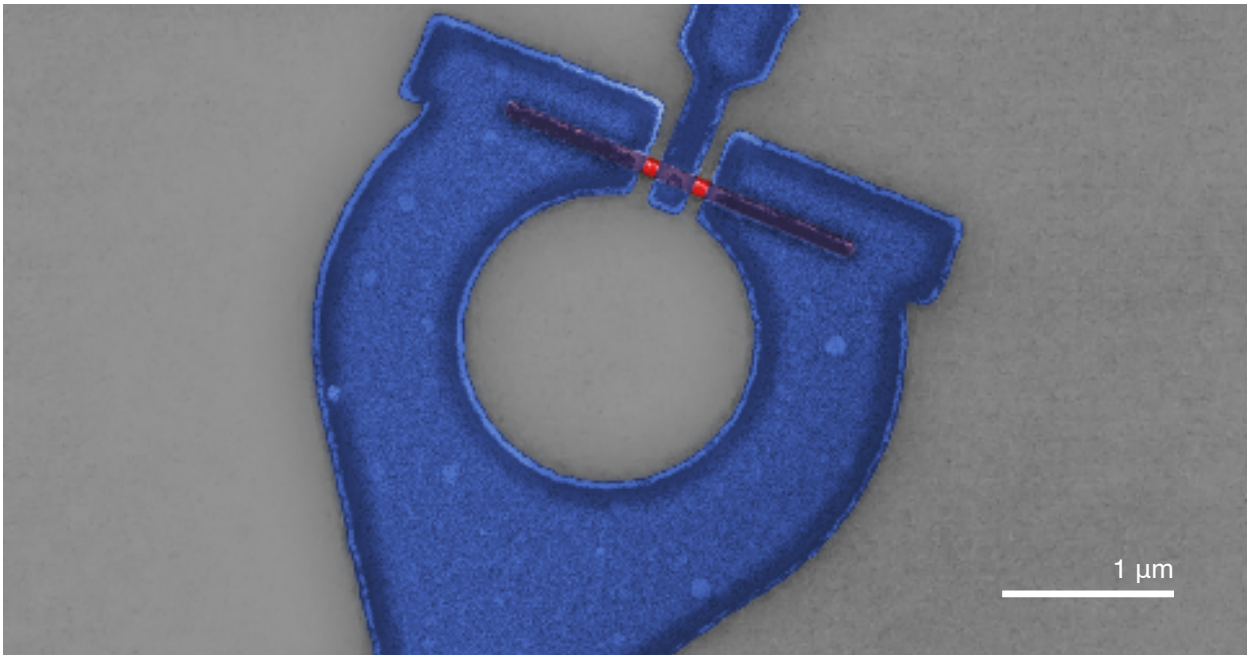

FIG. S9. Low magnification SEM image of the device shown in Fig. 1c of the main text.

[1] Gomes, U. P., Ercolani, D., Zannier, V., Beltram, F. & Sorba, L. Controlling the diameter distribution and density of InAs nanowires grown by Au-assisted methods. *Semicond. Sci. Technol.* **30**, 115012 (2015).

[2] Wallentin, J. & Borgström, M. T. Doping of semiconductor nanowires. *Journal of Materials Research* **26**, 2142–2156 (2011).

[3] Iorio, A. *et al.* Vectorial Control of the Spin–Orbit Interaction in Suspended InAs Nanowires. *Nano Lett.* **19**, 652–657 (2019).

[4] Rogachev, A. *et al.* Magnetic-Field Enhancement of Superconductivity in Ultranarrow Wires. *Physical Review Letters* **97**, 137001 (2006).

[5] Sapkota, K. R., Maloney, F. S. & Wang, W. Observations of the Kondo effect and its coexistence with ferromagnetism in a magnetically undoped metal oxide nanostructure. *Phys. Rev. B* **97**, 144425 (2018).

[6] Kondo, J. Resistance Minimum in Dilute Magnetic Alloys. *Prog. Theor. Phys.* **32**, 37–49 (1964).

[7] Bid, A., Bora, A. & Raychaudhuri, A. K. Temperature dependence of the resistance of metallic nanowires of diameter $\geqslant$ 15 nm: Applicability of bloch-grüneisen theorem. *Phys. Rev. B* **74**, 035426 (2006).

[8] Goldhaber-Gordon, D. *et al.* From the Kondo Regime to the Mixed-Valence Regime in a Single-Electron Transistor. *Phys. Rev. Lett.* **81**, 5225–5228 (1998).

[9] Parks, J. J. *et al.* Mechanical control of spin states in spin-1 molecules and the underscreened kondo effect. *Science* **328**, 1370–1373 (2010).

[10] Mallet, F. *et al.* Scaling of the Low-Temperature Dephasing Rate in Kondo Systems. *Phys. Rev. Lett.* **97**, 226804 (2006).

[11] Costi, T. A. *et al.* Kondo Decoherence: Finding the Right Spin Model for Iron Impurities in Gold and Silver. *Phys. Rev. Lett.* **102**, 056802 (2009).

[12] Hamann, D. R. New Solution for Exchange Scattering in Dilute Alloys. *Phys. Rev.* **158**, 570–580 (1967).

[13] Bergeret, F. S. & Tokatly, I. V. Theory of diffusive φ_0 Josephson junctions in the presence of spin-orbit coupling. *EPL* **110**, 57005 (2015).

[14] Konschelle, F., Tokatly, I. V. & Bergeret, F. S. Theory of the spin-galvanic effect and the anomalous phase shift φ_0 in superconductors and Josephson junctions with intrinsic spin-orbit coupling. *Phys. Rev. B* **92**, 125443 (2015).

[15] Buzdin, A. Direct coupling between magnetism and superconducting current in the josephson φ_0 junction. *Phys. Rev. Lett.* **101**, 107005 (2008).

[16] Clarke, J. & Braginski, A. I. (eds.) *The SQUID handbook* (Wiley-VCH, Weinheim, 2004).

[17] D'Ambrosio, S., Meissner, M., Blanc, C., Ronzani, A. & Giazotto, F. Normal metal tunnel junction-based superconducting quantum interference proximity transistor. *Applied Physics Letters* **107**, 113110 (2015).

[18] Golod, T., Rydh, A. & Krasnov, V. M. Detection of the phase shift from a single abrikosov vortex. *Phys. Rev. Lett.* **104**, 227003 (2010).